INTERNATIONAL JOURNAL OF PRECISION ENGINEERING AND MANUFACTURING Vol. 16, No. 12, pp. 2467-2474

DOI: 10.1007/s12541-015-0317-5
ISSN 2234-7593 (Print) / ISSN 2005-4602 (Online)

Numerical Investigation on Electromagnetism and Heat Transfer in Electroslag Remelting Process with Triple-Electrode

Qiang Wang[1], Fengsheng Qi[1], Fang Wang[1], and Baokuan Li[1,#]

1 School of Materials and Metallurgy, Northeastern University, 3-11, Wenhua Road, Shenyang, 110819, China
Corresponding Author / E-mail: libk@smm.neu.edu.cn, TEL: +86-24-83672216, FAX: +86-24-22906316

KEYWORDS: Electroslag remelting process, Triple-electrode, Joule heating, Heat transfer, Solidification

A transient three-dimensional (3D) model is developed for understanding the electromagnetism, heat transfer and phase change in electroslag remelting (ESR) furnace with triple-electrode. The electromagnetic fields are solved by Maxwell's equations using the finite element method. The temperature field and phase change are modeled by the enthalpy approach. A reasonable agreement is obtained between experiment and simulation. The electric current flows from one electrode into the slag and comes out from other two electrodes. Most electric current travels through the slag near the slag/ingot interface. A great amount of the Joule heating is generated by the slag and a higher value is found in the slag around the three electrodes. The highest temperature is located at the center of the slag layer. Increase in the current causes the increase in the Joule heating. A hotter slag and a deeper metal pool therefore are formed. The total Joule heating in the slag increases with more slag, while the average Joule heating density reduces. The metal pool depth increases and then decreases with the increasing slag thickness, and the deepest metal pool is obtained at the slag thickness of 200 mm. The power efficiency and the slag temperature reduce with the increasing electrode immersion depth. A shallower electrode immersion depth is a better choice for the ESR process with triple-electrode.

Manuscript received: April 9, 2015 / Revised: August 29, 2015 / Accepted: September 9, 2015

NOMENCLATURE

$\vec{A}$ = magnetic potential vector
$\vec{B}$ = magnetic flux density
C_l = specific heat of liquid metal
C_S = specific heat of solid metal
$\vec{E}$ = electric field intensity
$\vec{F}$ = Lorentz force
f_l = liquid fraction
H = enthalpy
$\vec{J}$ = current density
k_{eff} = effective thermal conductivity
Q = Joule heating
T = temperature
t = time
ρ = density
σ = electrical conductivity

1. Introduction

Electroslag remelting (ESR) process is an advanced technology of ingot production used in applications such as aeronautics, power generation, and tooling.[1] Simple structure and high reliability allows the ESR furnace with single electrode to be the most widely used unit nowadays. However, there are limitations to the unit with single electrode as the increasing ingot diameter. Due to a deeper metal pool and a wider mushy zone, segregation level tends to increase during the solidification process.[2,3] ESR furnace with triple-electrode therefore is proposed for reduce the segregation and produce a sound heavy ingot.[4] Fig. 1 shows the schematic of the ESR process with triple-electrode.

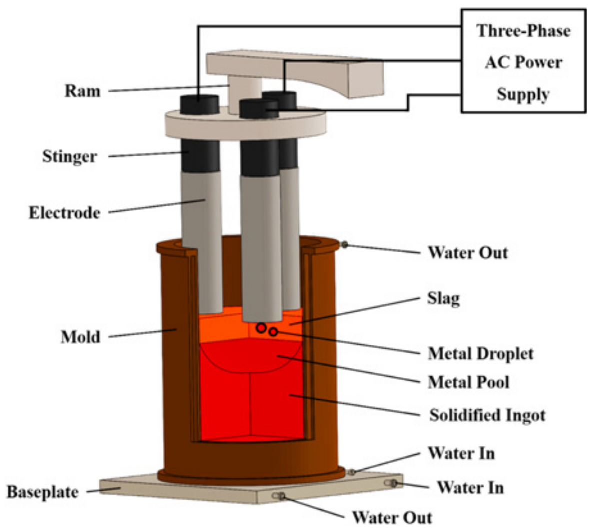

Fig. 1 Schematic of the ESR furnace with triple-electrode

Three electrodes are all inserted into a calcium fluoride based molten slag, and three-phase alternating current (AC) is applied. Joule heating is created in the slag because of the large electrical resistance, which is sufficient to melt the electrodes. The interaction between the self-induced magnetic field and AC gives rise to Lorentz force. Metal droplets sink through the less dense slag to form a liquid metal pool in the water-cooled mold. Chemical refining occurs in the molten slag as the metal droplets fall. Heat is lost to the mold, solidifying the metal and forming an ingot with dendritic structure, which maintains a shallow liquid metal pool throughout the process.[5]

In order to spread the application of the furnace with triple-electrode, a deeper understanding should be developed. Given the complicated phenomena involved, and the difficulty and expense of performing experiments on a real apparatus, numerical simulations constitute an attractive approach. In the past, efforts have been devoted to study the coupled electromagnetic, flow and temperature fields in the ESR process with single electrode.[6-9] A great difference however is observed in the furnace with multi-electrode. Dong et al. developed a coupled model using finite element method to investigate the electromagnetism, flow and heat transfer in the ESR process with four electrodes.[10] The metal pool in the furnace with four smaller electrodes was shallower than that in the unit with one larger electrode. Nevertheless, the critical part for the process, the current path, was not clarified. The electromagnetic fields and metal pool profiles in the ESR process with two electrodes were numerically described by Li et al.[11] Main part of the current flows through the slag, while few current enters into the ingot. Moreover, they indicated that the current, slag thickness and electrode immersion depth significantly influence the heat transfer.

As mentioned above, there is currently a lack of works concerning the complicated phenomena in the ESR process with triple-electrode. The present work aims to develop a transient 3D mathematical model of the ESR process with triple-electrode. The electromagnetism, heat transfer and phase change are clarified. The effects of the current, the slag thickness and the immersion depth of the electrode on the metal pool depth are investigated. An experimental measurement has been conducted to validate the model.

2. Mathematical Formulation

2.1 Assumptions

In order to limit the computational time, the model relies on the following assumptions:

(1) Fluid flow and metal droplet are not considered although these should be included for the sake of the completeness.[12]

(2) The mold is not taken into account. The computation domain consists of the electrodes, the slag, the ingot and the surrounding air.

(3) The slag electrical conductivity depends on the temperature. The other physical properties are constant.[13]

(4) The solidification shrinkage is neglected.[14]

2.2 Electromagnetic phenomena

The electromagnetic fields are described by Maxwell's equations.[15] The current displacement is much lower than the electrical conduction, because the electrical conductivities of the slag and the metal are not too small.[16] Due to the absence of the fluid flow, the current density can be expressed:

$$\vec{J} = \sigma\vec{E} \tag{1}$$

At the same time, the magnetic potential vector is related to the magnetic field by:[17]

$$\vec{B} = \nabla \times \vec{A} \tag{2}$$

The time-averaged Lorentz force and Joule heating therefore are described:[18]

$$\vec{F} = \vec{J} \times \vec{B} \tag{3}$$

$$Q = \frac{\vec{J}\cdot\vec{J}}{\sigma} \tag{4}$$

2.3 Heat transfer and phase change

To obtain a precise prediction of the temperature distribution and phase change, the energy conservation equation of the enthalpy-formulation is employed:[19]

$$\frac{\partial H}{\partial t} = \nabla \cdot (k_{eff} \nabla T) + Q \tag{5}$$

The melting of the electrode and the solidification of the ingot happen simultaneously in the process and are described by the definition of the enthalpy:[20]

$$H(T) = \rho(1-f_l)\int_{T_{ref}}^{T} c_s dT + \rho f_l\left(\int_{T_{ref}}^{T} c_s dT + L + \int_{T_s}^{T} c_l dT\right) \tag{6}$$

2.4 Boundary conditions

Three-phase AC is imposed at the top surfaces of the three electrodes.

Table 1 Physical properties, geometrical and operating conditions of the ESR system

Parameter	Value
Physical properties of metal	
Density, kg/m^3	7500
Liquidus/solidus temperature, K	1623/1458
Latent heat of fusion, kJ/kg	270
Thermal conductivity, W/(m·K)	30.52
Specific heat, J/(kg·K)	752
Electrical conductivity, $^{-1}$·m^{-1}	7.14×10^5
Magnetic permeability, H/m	1.257×10^{-6}
Physical properties of slag	
Density, kg/m^3	2800
Liquidus temperature, K	1633
Thermal conductivity, W/(m·K)	10.46
Specific heat, J/(kg·K)	1255
Electrical conductivity, $^{-1}$·m^{-1}	$\ln\sigma = -6769.0/T+8.818$
Magnetic permeability, H/m	1.257×10^{-6}
Geometry	
Electrodes diameter, m	0.45
Electrodes height, m	1
Ingot diameter, m	1.6
Ingot height, m	2
Slag height, m	0.15/0.2/0.25/0.3/0.35
Immersion depth of electrodes, m	0.02/0.05/0.08
Operating conditions	
Current, A	12500/15000/17500
Frequency, Hz	50
Temperature of cooling water in and out, K	288/310
Temperature of air, K	298

A zero potential is applied at the ingot bottom.[21] The lateral walls of the electrodes, the slag and the ingot as well as the slag top surface are assumed to be electrically insulated. Besides, the magnetic flux parallel condition is used at the outer surface of the air region.[13]

The whole air is set as the room temperature. The top surface of the slag exchanges heat with the air by both natural convection and thermal radiation. The heat transfer between the lateral walls of electrodes and air are carried out by natural convection.[22] Equivalent heat transfer coefficients are deduced from literature and experiment.[23] Zero temperature gradient is applied on the electrodes top surfaces. The detailed physical properties, geometrical and operating conditions are listed in Table 1.[24,25]

3. Numerical Implementation

The simulation is executed by the commercial code ANSYS MECHANICAL APDL 12.0 based on the finite element method.[18] The governing equations for the electromagnetism, heat transfer and phase change are simultaneously solved using an iterative procedure. Before advancing to the next time step, the iterative procedure is continued until all normalized unscaled residuals are less than 10^{-6}. Solid 97 element is adopted to calculate the electromagnetic fields, and Solid 70 is employed for the heat transfer and phase change. They all consist of eight nodes providing enough accuracy. The domain except the air region is discretized by the hexahedral elements as shown in Fig. 2.

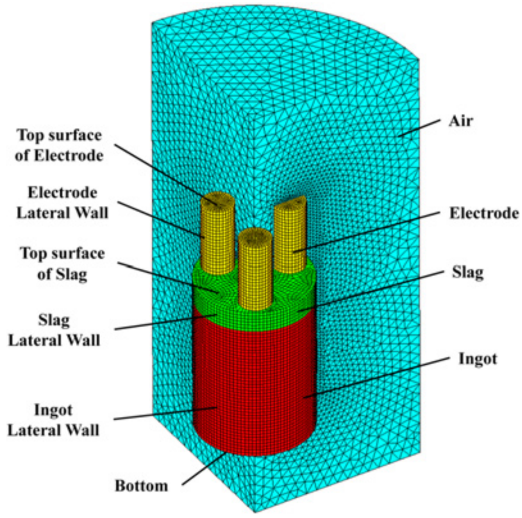

Fig. 2 Mesh model used in the present work

Mesh independence is thoroughly tested. Three families of meshes are generated, respectively with 1,850,000, 2,110,000 and 2,420,000 finite elements. After a typical simulation, we compare the temperature of three points in the slag. The deviation of the simulated results between the first and second mesh is about 7%, while approximately 3% between the second and third mesh. Considering the expensive computation, the second mesh therefore is retained for the rest of the present work. A typical simulation with 0.002 seconds time step runs around 46 hours using 4 cores of 3.30 GHz.

4. Model Validation

The geometrical and operation conditions of the experiment facility are the same as that of the numerical simulation. The slag composition is composed of the calcium fluoride, 75 mass pct, and the aluminum oxide, 25 mass pct. The slag thickness is constant at 250 mm. The current is 15000 A with a frequency of 50 Hz. We measured the magnetic flux density of points in the air around the three electrodes using a Gauss meter SHT-6 and the temperature of points in the slag by a disposable W3Re/W25Re thermocouple. Figs. 3(a) and 3(b) display the comparison of the magnetic flux density and temperature between the experimental measurements and numerical results. Relatively larger discrepancy of the measured magnetic flux density from the simulated one is observed close to the electrode lateral wall, because the higher temperature would reduce the accuracy of the Gauss meter. Measured temperatures at point 2 are lower than the calculated results, because the motion of slag ignored in the present work promotes the heat loss. A reasonable agreement is obtained indicating the reliability of the model.

5. Results and Discussion

Fig. 4 illustrates the current density fields in the two planes at 6000 s. The current, the slag thickness and the electrode immersion depth are 15000 A, 250 mm and 50 mm, respectively. It can be seen that the

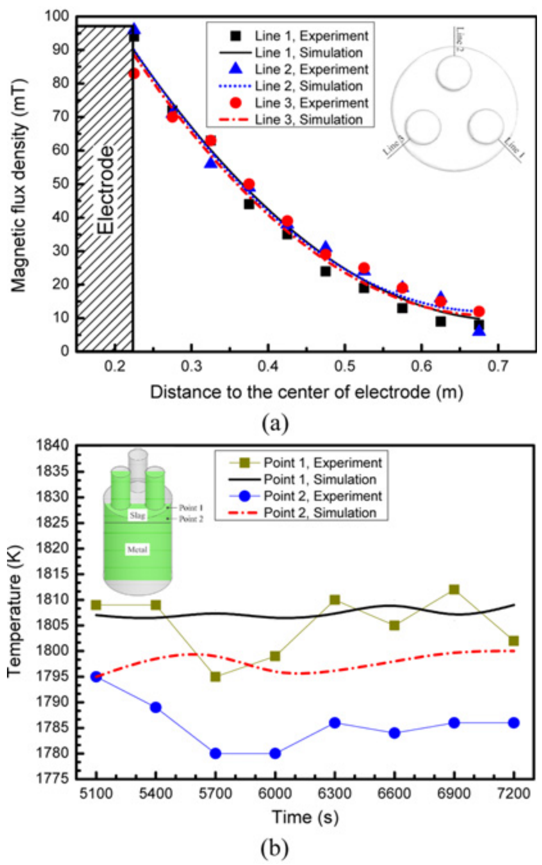

Fig. 3 (a) Comparison of the magnetic flux density between the measurements and simulations. Line 1, 2 and 3 are 0.4 m above the top surface of the slag, and (b) comparison of the temperature between the measurements and simulations

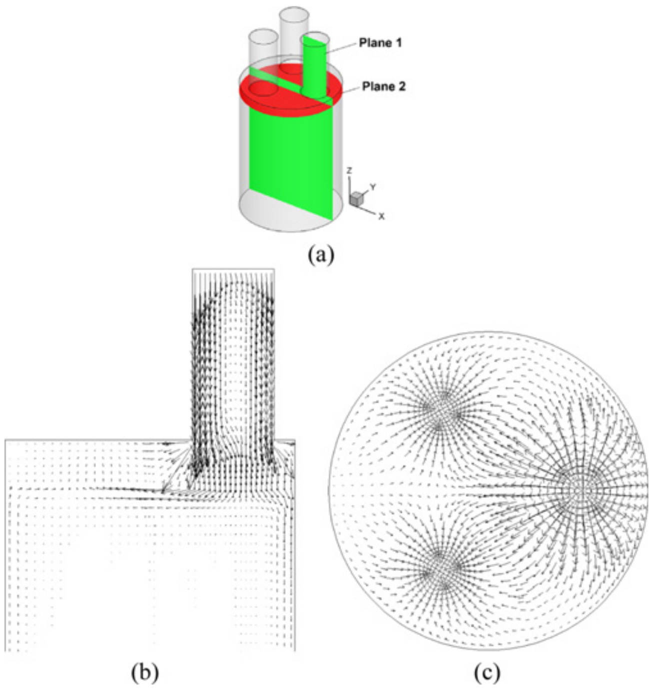

Fig. 4 (a) Schematic of the plane 1 (Y = 0) and plane 2 (located at the middle of the slag layer), (b) and (c) the current density fields in the plane 1 and 2 at 6000 s, and the maximum current density is around 1.8×10^5 A/m^2. The current is 15000 A, the slag thickness is 250 mm and the electrode immersion depth is 50 mm

electric current flows from one electrode into the slag and comes out from other two electrodes. The current loop is different from that in the ESR furnace with single electrode, where the current passes from the electrode to the baseplate.[18] Due to the skin effect, the electric current tends to concentrate at the periphery of the electrodes. Moreover, the current density at the left side is larger than that at the right side as a result of the neighbor effect. In addition, the metal pool and ingot can be regard as the neutral point in the furnace because of the higher electrical conductivity. As a result, the downward electric current turns at the slag/ingot interface. Most electric current travels through the slag near the slag/ingot interface, and only a small part, less than 10 pct, enters into the ingot.

Fig. 5 demonstrates the distribution of the Joule heating density. The distribution of the Joule effect is similar to that of the current density, because it is determined by the electric current. A great amount of the Joule heating is created in the slag which owns a lower electrical conductivity. Moreover, a higher value of the Joule heating is found in the slag around the electrodes.

The slag is hotter than the ingot as shown in Fig. 6. The highest temperature is located at the center of the slag where the temperature is more uniform. The temperature of the slag decreases along the radial direction. The outer slag is colder under the cooling effect. Additionally, lots of heat is extracted by the cooling water at the bottom. A larger

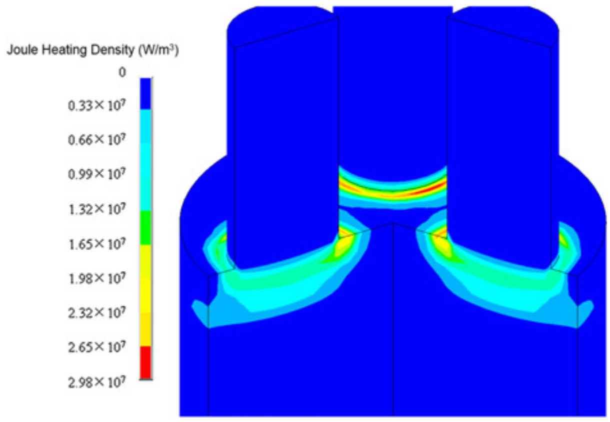

Fig. 5 Distribution of the Joule heating density at 6000 s. The current is 15000 A, the slag thickness is 250 mm and the electrode immersion depth is 50 mm

axial temperature gradient is formed at the lower part of the ingot. The influence of the cooling water at the bottom however decays as solidification progresses. The effect of the cooling at the lateral wall advantages over the impact of the cooling at the bottom resulting in a more uniform temperature at the middle of the ingot.

The heat extracted by the cooling water drives the freezing of metal. A liquid metal pool is formed as shown in Fig. 7, and the depth is approximately 0.3 diameter of the mold. A shallower metal pool is well received indicating that the furnace with triple-electrode is beneficial to

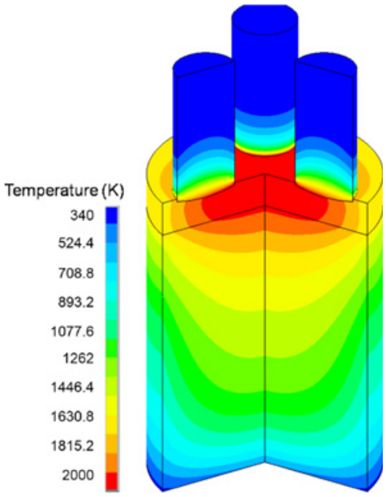

Fig. 6 Distribution of the temperature at 6000 s. The current is 15000 A, the slag thickness is 250 mm and the electrode immersion depth is 50 mm

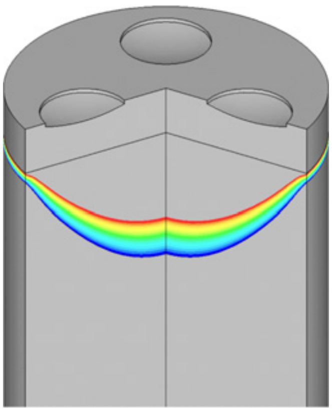

Fig. 7 Metal pool profile at 6000 s. The current is 15000 A, the slag thickness is 250 mm and the electrode immersion depth is 50 mm

the manufacture of the large ingot.

Fig. 8 reveals the effects of the current and the slag thickness on the total Joule heating and the average Joule heating density in the slag region. As expected, the total Joule heating as well as the average Joule heating density becomes larger with the increasing current. The rule however is going to be different when we change the slag thickness. The average Joule heating density in the slag reduces with a thicker slag layer although the total Joule heating increases. For instance, the total Joule effect increases from 1.24×10^6 W to 1.87×10^6 W while the average Joule heating density goes down from 3.31×10^6 W/m^3 to 2.10×10^6 W/m^3 with the slag thickness ranging from 150 mm to 350 mm at the current of 15000 A. The heat production efficiency reduces with a thicker slag cap, because the Joule heating uniformity decreases and more heat is carried away by the cooling water. Fig. 9 indicates the effects of current and slag thickness on the maximal temperature. The highest temperature increases with the increase of the current and slag thickness owning to more heat. The maximum depth of the metal pool however increases and then decreases with the increasing slag thickness

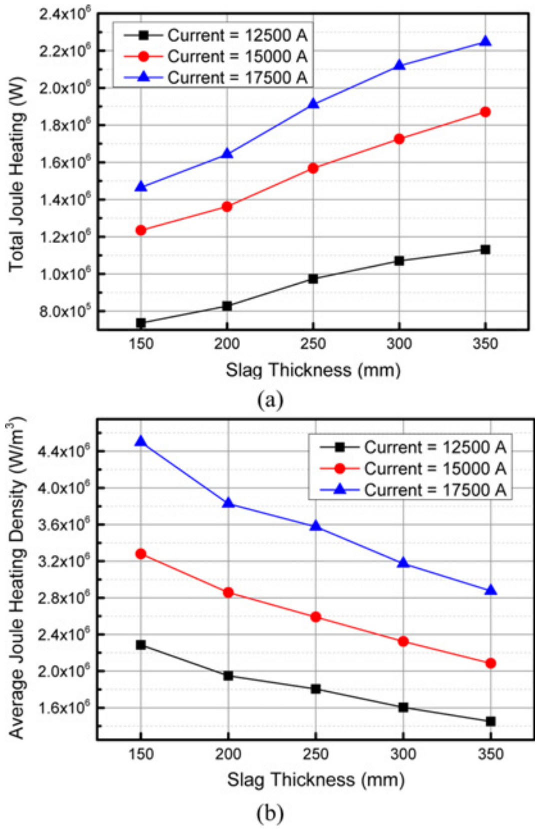

Fig. 8 (a) Effects of the current and slag thickness on the total Joule heating in the slag, (b) effects of the current and slag thickness on the average Joule heating density in the slag, and the electrode immersion depth is 50 mm

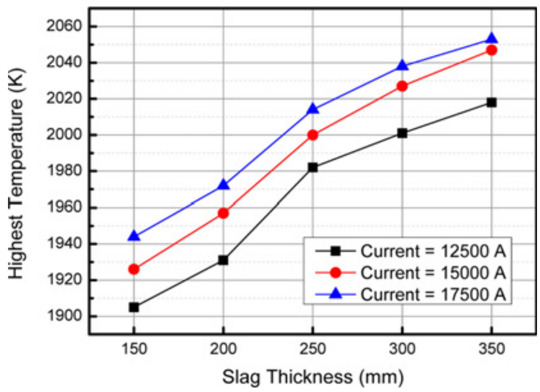

Fig. 9 Effects of the current and slag thickness on the highest temperature, and the electrode immersion depth is 50 mm

as shown in Fig. 10. The deepest metal pool is obtained when the slag thickness is 200 mm with the three currents. The combined effect of the total Joule heating and the slag thermal resistance is responsible for it. Less slag cannot provide enough heat, and a deeper metal pool is formed with more slag. Nevertheless, the thermal resistance of the slag significantly appears if the slag thickness continuous to increase. The thicker slag blocks the heat transfer downward yielding a shallower metal pool.

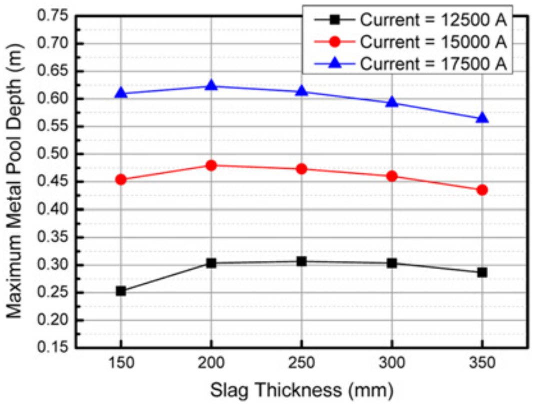

Fig. 10 Effects of the current and slag thickness on the maximum metal pool depth, and the electrode immersion depth is 50 mm

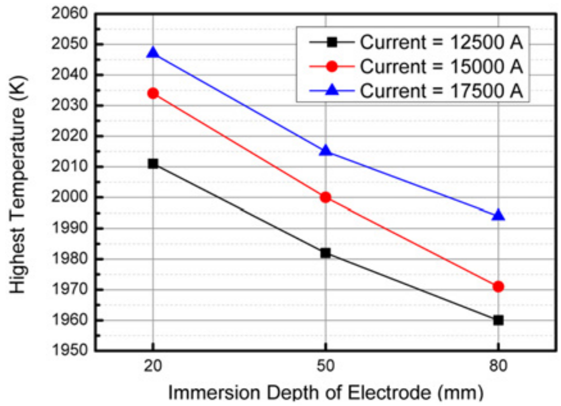

Fig. 12 Effects of the current and electrode immersion depth on the highest temperature, and the slag thickness is 250 mm

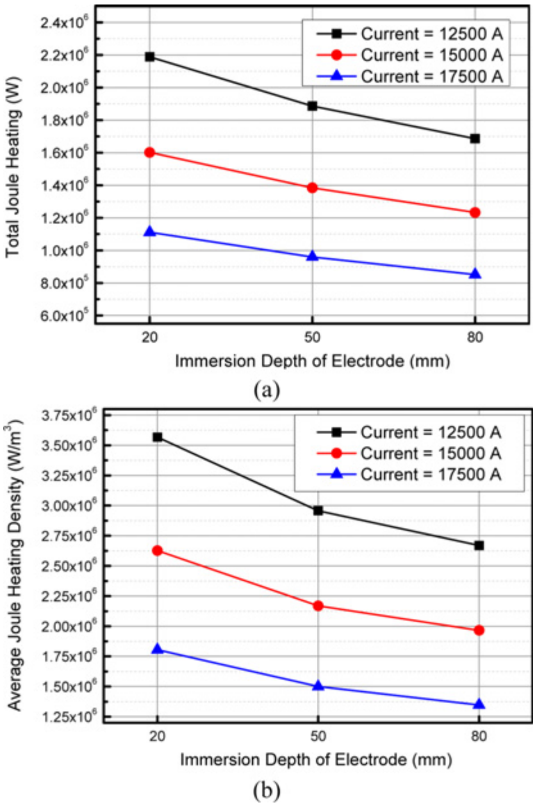

Fig. 11 (a) Effects of the current and electrode immersion depth on the total Joule heating in the slag, (b) effects of the current and electrode immersion depth on the average Joule heating density in the slag, and the slag thickness is 250 mm

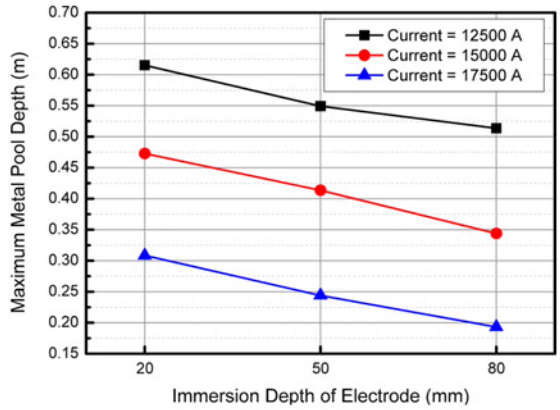

Fig. 13 Effects of the current and electrode immersion depth on the maximum metal pool depth, and the slag thickness is 250 mm

Fig. 11 represents the effect of the current and the electrode immersion depth on the total Joule heating and the average Joule heating density in the slag region. The total Joule heating as well as the average Joule heating density decreases with the increasing electrode immersion depth, because the electric current passes though fewer slag. The highest temperature therefore reduces as shown in Fig. 12 indicating that larger immersion depth would reduce the power efficiency. Due to the less heat and the constant slag thickness, the metal pool volume definitely decreases leading to a shallower metal pool as illustrated in Fig. 13. It can be deduced that smaller immersion depth of the electrode is a better choice in the practice of the ESR process with triple-electrode.

6. Conclusions

(1) A transient 3D model is established to investigate the electromagnetism, heat transfer and phase change in the ESR furnace with triple-electrode. The effects of the current, the slag thickness and the immersion depth of the electrode on the metal pool depth are clarified. The simulation closely agrees the experiment.

(2) The electric current flows from one electrode into the slag and comes out from other two electrodes. Most electric current travels through the slag near the slag/ingot interface, and only a small part, less than 10 pct, enters into the ingot.

(3) A great amount of the Joule heating is created by the slag and a higher value is observed in the slag around the three electrodes. The slag temperature is higher than that of the ingot and the highest temperature is located at the center of the slag.

(4) Increase in the current causes the increase in the Joule heating. A hotter slag and a deeper metal pool therefore are formed providing more opportunities for the macrosegregation.
(5) The total Joule heating in the slag increases with more slag, while the average Joule heating density reduces. The metal pool depth increases and then decreases with the increasing slag thickness, and the deepest metal pool is obtained at the slag thickness of 200 mm.
(6) The power efficiency and the slag temperature reduce with the increasing electrode immersion depth. A shallower electrode immersion depth is a better choice for the ESR process.

ACKNOWLEDGEMENT

The authors' gratitude goes to National Natural Science Foundation of People's Republic of China (No. 51210007) and Fundamental Research Funds of People's Republic of China for the Central Universities (N140206002).

REFERENCES

1. Hernandez-Morales, B., and Mitchell, A., "Review of Mathematical Models of Fluid Flow, Heat Transfer, and Mass Transfer in Electroslag Remelting Process," Ironmaking & Steelmaking, Vol. 26, No. 6, pp. 423-438, 1999.
2. Li, J., Wu, M., Ludwig, A., and Kharicha, A., "Simulation of Macrosegregation in a 2.45-Ton Steel Ingot using a Three-Phase Mixed Columnar-Equiaxed Model," International Journal of Heat and Mass Transfer, Vol. 72, pp. 668-679, 2014.
3. Založnik, M. and Combeau, H., "Thermosolutal Flow in Steel Ingots and the Formation of Mesosegregates," International Journal of Thermal Sciences, Vol. 49, No. 9, pp. 1500-1509, 2010.
4. Ferng, Y. M., Chieng, C. C., and Pan, C., "Numerical Simulations of Electro-Slag Remelting Process," Numerical Heat Transfer, Vol. 16, No. 4, pp. 429-449, 1989.
5. Gu, J. P. and Beckermann, C., "Simulation of Convection and Macrosegregation in a Large Steel Ingot," Metallurgical and Materials Transactions A, Vol. 30, No. 5, pp. 1357-1366, 1999.
6. Weber, V., Jardy, A., Dussoubs, B., Ablitzer, D., Rybéron, S., et al., "A Comprehensive Model of the Electroslag Remelting Process: Description and Validation," Metallurgical and Materials Transactions B, Vol. 40, No. 3, pp. 271-280, 2009.
7. Ludwig, A., Kharicha, A., and Wu, M., "Modeling of Multiscale and Multiphase Phenomena in Materials Processing," Metallurgical and Materials Transactions B, Vol. 45, No. 1, pp. 36-43, 2014.
8. Jardy, A., Ablitzer, D., and Wadier, J. F., "Magnetohydronamic and Thermal Behavior of Electroslag Remelting Slags," Metallurgical Transactions B, Vol. 22, No. 1, pp. 111-120, 1991.
9. Fezi, K., Yanke, J., and Krane, M. J., "Modeling Macrosegregation during Electroslag Remelting of Alloy 625," Proc. of the International Symposium on Liquid Metal Processing and Casting (LMPC), pp. 151-158, 2013.
10. Dong, Y., Jiang, Z., Liu, H., Chen, R., and Song, Z., "Simulation of Multi-Electrode Esr Process for Manufacturing Large Ingot," ISIJ International, Vol. 52, No. 12, pp. 2226-2234, 2012.
11. Li, B., Wang, B., and Tsukihashi, F., "Modeling of Electromagnetic Field and Liquid Metal Pool Shape in an Electroslag Remelting Process with Two Series-Connected Electrodes," Metallurgical and Materials Transactions B, Vol. 45, No. 3, pp. 1122-1132, 2014.
12. Kharicha, A., Ludwig, A., and Wu, M., "Shape and Stability of the Slag/Melt Interface in a Small Dc Esr Process," Materials Science and Engineering: A, Vols. 413-414, pp. 129-134, 2005.
13. Mitchell, A. and Hernandez-Morales, B., "Electromagnetic Stirring with Alternating Current during Electroslag Remelting," MTB, Vol. 21, No. 4, pp. 723-731, 1990.
14. Mitchell, A., "Solidification in Remelting Processes," Materials Science and Engineering: A, Vols. 413-414, pp. 10-18, 2005.
15. Kelkar, K. M., Patankar, S. V., and Mitchell, A., "Computational Modeling of the Electroslag Remelting (ESR) Process Used for the Production of Ingots of High-Performance Alloys," Proc. of the International Symposium on Liquid metal Processing and Casting, pp. 137-144, 2005.
16. Dilawari, A. H. and Szekely, J., "Heat Transfer and Fluid Flow Phenomena in Electroslag Refining," Metallurgical Transactions B, Vol. 9, No. 1, pp. 77-87, 1978.
17. Biro, O. and Preis, K., "On the Use of the Magnetic Vector Potential in the Finite-Element Analysis of Three-Dimensional Eddy Currents," IEEE Transactions on Magnetics, Vol. 25, No. 4, pp. 3145-3159, 1989.
18. Li, B., Wang, F., and Tsukihashi, F., "Current, Magnetic Field and Joule Heating in Electroslag Remelting Processes," ISIJ International, Vol. 52, No. 7, pp. 1289-1295, 2012.
19. Zhao, R., Gosselin, L., Fafard, M., and Ziegler, D. P., "Heat Transfer in Upper Part of Electrolytic Cells: Thermal Circuit and Sensitivity Analysis," Applied Thermal Engineering, Vol. 54, No. 1, pp. 212-225, 2013.
20. Wang, Q., Zhao, R., Fafard, M., and Li, B., "Three-Dimensional Magnetohydrodynamic Two-Phase Flow and Heat Transfer Analysis in Electroslag Remelting Process," Applied Thermal Engineering, Vol. 80, pp. 178-186, 2015.
21. Wang, Q., He, Z., Li, B., and Tsukihashi, F., "A General Coupled Mathematical Model of Electromagnetic Phenomena, Two-Phase Flow, and Heat Transfer in Electroslag Remelting Process including Conducting in the Mold," Metallurgical and Materials Transactions B, Vol. 45, No. 6, pp. 2425-2441, 2014.
22. Yanke, J. and Krane, M. J. M., "A Parametric Study of Slag Skin Formation in Electroslag Remelting," Proc. of the International

Symposium on Liquid Metal Processing and Casting, pp. 71-78, 2013.

23. Hugo, M., Dussoubs, B., Jardy, A., Escaffre, J., and Poisson, H., "Impact of the Solidified Slag Skin on the Current Distribution during Electroslag Remelting," Proc. of the International Symposium on Liquid Metal Processing and Casting, pp. 79-85, 2013.

24. Patel, A. D., "Effect of Electrode Pipe and Mold Current on Electromagnetic Fields in Esr," Proc. of International Symposium on Liquid Metal Processing and Casting LMPC, pp. 95-100, 2007.

25. Kharicha, A., Schutzenhofer, W., Ludwig, A., Tamer, R., and Wu, M., "On the Importance of Electric Currents Flowing Directly into the Mould During an Esr Process," Steel Research International, Vol. 79, No. 8, pp. 632-636, 2008.